

Determination of the optical properties of cholesteatoma in the spectral range of 250 to 800 nm

ERIC L. WISOTZKY,^{1,2,4,5}  PHILIPP ARENS,^{3,4}  STEFFEN DOMMERICH,³ ANNA HILSMANN,¹ PETER EISERT,^{1,2} AND FLORIAN C. UECKER³

¹Fraunhofer Heinrich-Hertz-Institute, Computer Vision and Graphics, Berlin, Germany

²Humboldt-Universität zu Berlin, Visual Computing, Berlin, Germany

³Charité - Universitätsmedizin Berlin, Department of Otorhinolaryngology, Berlin, Germany

⁴Eric L. Wisotzky and Philipp Arens contribute as joint first author

⁵eric.wisotzky@hhi.fraunhofer.de

Abstract: Cholesteatoma of the ear can lead to life-threatening complications and its only treatment is surgery. The smallest remnants of cholesteatoma can lead to recurrence of this disease. Therefore, the optical properties of this tissue are of high importance to identify and remove all cholesteatoma during therapy. In this paper, we determine the absorption coefficient μ_a and scattering coefficient μ_s' of cholesteatoma and bone samples in the wavelength range of 250 nm to 800 nm obtained during five surgeries. These values are determined by high precision integrating sphere measurements in combination with an optimized inverse Monte Carlo simulation (iMCS). To conserve the optical behavior of living tissues, the optical spectroscopy measurements are performed immediately after tissue removal and preparation. It is shown that in the near-UV and visible spectrum clear differences exist between cholesteatoma and bone tissue. While μ_a is decreasing homogeneously for cholesteatoma, it retains at the high level for bone in the region of 350 nm to 580 nm. Further, the results for the cholesteatoma measurements correspond to published healthy epidermis data. These differences in the optical parameters reveal the future possibility to detect and identify, automatically or semi-automatically, cholesteatoma tissue for active treatment decisions during image-guided surgery leading to a better surgical outcome.

© 2020 Optical Society of America under the terms of the [OSA Open Access Publishing Agreement](#)

1. Introduction

Cholesteatoma, due to its destructive growth can lead to life-threatening complications and its only treatment is surgery. It requires a complete resection to avoid a recurrence. Cholesteatoma is defined by squamous epithelium in the middle ear spaces. Its further growth in the middle ear and into the adjacent structures leads to life-threatening complications. The destruction of the ossicles and cochlea can cause hearing loss and can lead to deafness. An erosion of the facial canal can lead to facial paralysis. Disturbances of the organ of equilibrium may be due to semicircular fistulas. Fortified inflammation causes mastoiditis, meningitis, intracranial abscesses and sinus vein thrombosis [1–4]. Cholesteatoma can occur at any age and has an incidence of about 10 per 100,000 adults [5,6] with men 1.4 times more likely to be affected than women [1,7]. The objectives of surgical management of cholesteatoma include eradicating the disease while recovering or preserving the hearing. In cases of residual and recurrent cholesteatoma, a revision surgery is strictly needed.

The optical properties of human tissues, as skin or cholesteatoma, have an effect on diagnostic and therapeutic procedures. For example, the color of the human skin provides a subjective characteristic to visually diagnose a disease [8]. To objectify the diagnosis, measurements of the

optical properties have to be performed. Light enters and exits human tissue, which increases the interest of understanding the scattering and absorption properties of it, as it is the basis for objective medical diagnostics and therapy [9]. For this reason, the optical properties of various tissue types have been extensively investigated in recent years. In particular, different skin layers and types, blood and easily distinguishable tissue types, such as brain or liver, have been analyzed [8–10]. Occasionally, as for skin tissue, tumors have been examined as well [11]. Due to the fact that epithelium in general and the skin in particular lines the outer covering of organs and the body respectively, it protects the inner body structures against pathogens and is of large interest for medical diagnostics and therapy. Therefore, the optical properties of the individual skin layers, epidermis and dermis, as well as the entire composite are extensively analyzed in vitro and in vivo [8,12]. Specifying these optical properties is the initial step interpreting measurements correctly. Except for blood and skin, where extensive data is available, most of the studies analyze different tissue types only at few wavelengths mainly in the infra-red (IR). These results, however, are usually not applicable for settings using the visible range, as for intraoperative tissue analysis and treatment [13,14]. In order to allow a broad range of applications in the visible light range, a sophisticated analysis of optical tissue properties is necessary. One possible application for surgically relevant tissue differentiation would be the removal of cholesteatoma. A first example for intraoperative applications has been presented for endoscopic driven surgeries, where the narrow-band imaging-technique of blood vessels in mucosal structures has proven the potential of using wavelength-filtered light to enhance the diagnostic outcome of visual patient data [15]. This technique uses selected wavelengths in the visible range based on information available for blood in that range.

Histologically, cholesteatoma has the same four layers as in skin epidermis, basal, squamous, granulosum, and stratum corneum [7,16]. Therefore, the aim of this study is to derive a set of empirical formulations to predict the optical properties of cholesteatoma and bone, extracted during tympanomastoidectomy.

An established method to quantify optical properties of biochemical systems in the spectral range from ultra-violet (UV) to IR is optical absorption spectroscopy [17]. The optical properties of a tissue sample are described by the intrinsic optical parameters absorption coefficient μ_a (mm^{-1}), scattering coefficient μ_s (mm^{-1}) and the scattering phase function represented by the anisotropy factor g [18]. These parameters characterize tissue scattering in terms of the relative forward versus backward direction of scatter for thicker tissue samples (with multiple scattering events). An introduction to the optical properties is presented at [19].

In this study, an integrating sphere technique improved with optical lenses and combined with inverse Monte Carlo simulations (iMCS) [20–22] is used to determine the optical parameter μ_a , μ_s and g of the bone and cholesteatoma. An experimental setup is used that gave transmittance and reflectance measurements in the wavelength range from 250 nm to 800 nm under defined conditions. Due to the histological comparability of cholesteatoma and epidermis, the results of this study are compared with presented optical properties of the epidermis in literature.

2. Material and methods

2.1. Patients

The study was conducted with five patients, in the age of 14, 26, 38, 52 and 66 years. Each patient had a cholesteatoma, which is keratinizing squamous epithelium, occurring in the middle ear and mastoid, see Fig. 1. The only treatment for such patients is the complete surgical resection via tympanomastoidectomy [23]. The written informed consent of extracting cholesteatoma and bone samples during the standard procedure had been provided by all patients. The tissues were extracted individually, selected during the surgery by the clinician. Due to the individual anatomy of each patient the amount of extracted tissue differed, which resulted in different sample thicknesses d [24]. After spectroscopy, all taken samples were additionally analyzed

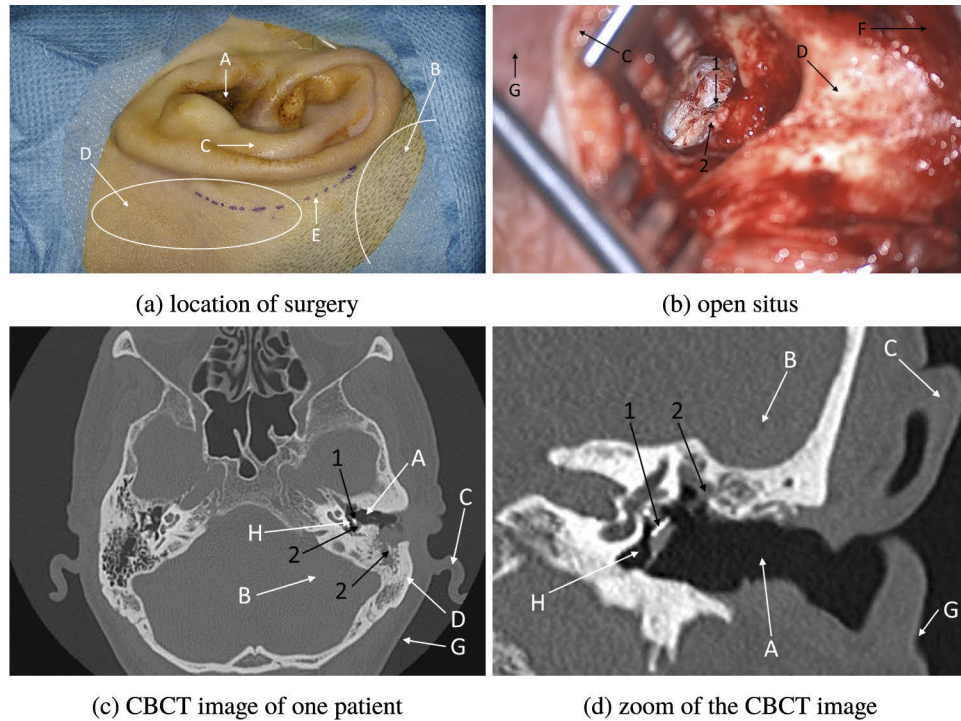


Fig. 1. These images show the location (a) and anatomy (b) of the interventions. An open situs, where all relevant tissue structures are visible, is shown in (b). The position of this situs is shown in the left image marked with the dashed incision line (E). The corresponding CBCT images (c) and (d) show the location of the cholesteatoma in the left ear. The labels describe: A - external ear canal, B - brain, C - catilage, D - mastoid bone, E - incision line, F - musculus temporalis, G - skin, H - middle ear, 1 - tympanic membrane with titanium prosthesis, 2 - cholesteatoma with bone arrosion.

using normal histological examination to confirm the specific tissue type. The whole study was in agreement with the ethical approval obtained from the Ethics Committee of the Charité – Universitätsmedizin Berlin.

2.2. Spectroscopic measurements

The tissue samples were prepared directly after being removed from the patient to fit on the cuvette, with a thickness between $87\ \mu\text{m}$ to $524\ \mu\text{m}$, depending on the sample quantity. The diameter of the prepared samples were between $5.3\ \text{mm}$ up to $15.0\ \text{mm}$. Immediately after the sample preparation the measurements were started. Thus, most measurements had been taken in the first two hours after removal to obtain the optical properties of living tissue. To show the effect of tissue degradation and its influence on the optical behavior, four samples were additionally analyzed at different time instants $t < 2\ \text{h}$, $t = 20\ \text{h}$ and $t = 90\ \text{h}$. The macroscopic optical parameters, diffuse reflectance R_d and the total transmission T_t were measured every $5\ \text{nm}$ in the spectral range from $250\ \text{nm}$ to $800\ \text{nm}$, with an integrating sphere UV/visible spectrophotometer (Lambda 650, PerkinElmer, Germany), which is a two-beam spectrometer with double monochromator system. This led to 111 datasets per measurement. The diameter of the incident light beam on the tissue sample was $4.5\ \text{mm}$ and the scan rate was $5\ \text{nm/s}$. The experimental setup had already been used and described in other studies [20,25]. Thus, a

schematic representation of the sphere setup used in this study can be found in Fig. 1 of Friebe et al. [20].

The light source consists of a deuterium lamp for the UV range and a wolfram halogen lamp for the visible/near infrared (VIS/NIR) range. The cuvette can be fixed in a defined position at a constant distance to the sphere aperture, in front or behind of the integrating sphere, to measure the transmittance spectra T_t or the reflectance spectra R_d , respectively. For the measurement of T_t , the reflectance port was closed with a diffuse reflecting Spectralon[®] standard with known reflectance spectrum. R_d was measured relatively to the reflectance standard by replacing the special Spectralon[®] by the sample. The Fresnel reflectance of the cuvette glass left the sphere through the open Fresnel port to avoid interference with the diffuse reflectance. This spectrophotometric setup allowed the measurement of macroscopic radiation distribution with an extremely reduced error potential [20].

2.3. Inverse Monte Carlo simulation

The optical parameters μ_a and $\mu'_s = \mu_s(1 - g)$ were obtained from the inverse Monte Carlo simulation (iMCS). The iMCS method, first presented by Roggan et al. [26], was adapted to the geometry of the measurement system [20] and used iteratively forward Monte Carlo simulation to calculate μ_a , μ_s and g from the measured reflection R_d and transmission T_t using a phase function [18]. For initialization, the iMCS used estimated μ_a , μ_s , and g from the Kubelka-Munk theory [20]. The forward simulation used the Newton-Raphson method [27] to find an approximation of $R_d(\mu_a, \mu_s, g)$ and $T_t(\mu_a, \mu_s, g)$. These approximated R_d and T_t were compared to the measured values. In case of significant difference, μ_a , μ_s , and g were varied and a next iteration of forward simulation took place until the difference between measured and simulated R_d and T_t stayed in the defined error margin. This process was repeated for all measured wavelengths. A detailed description of the used simulation sequences is described in Friebe et al. [20].

3. Results

3.1. Spectroscopic measurements

Forty-six fresh tissue samples obtained from five patients during the planned surgery were used for the measurements. The 28 cholesteatoma samples (examples are shown in Fig. 2) were varying in terms of thickness d and size r as described in Sec. 2.2 due to the occurrence in each individual patient. For the 18 bone sample (examples are shown in Fig. 3), two modalities were used due to the solid opaque structure. First, two solid bone fragments were analyzed in terms of reflection R_d only. Further, to achieve reflection R_d and transmission T_t data, the other 16 samples were bone chips, harvested from the drilling.

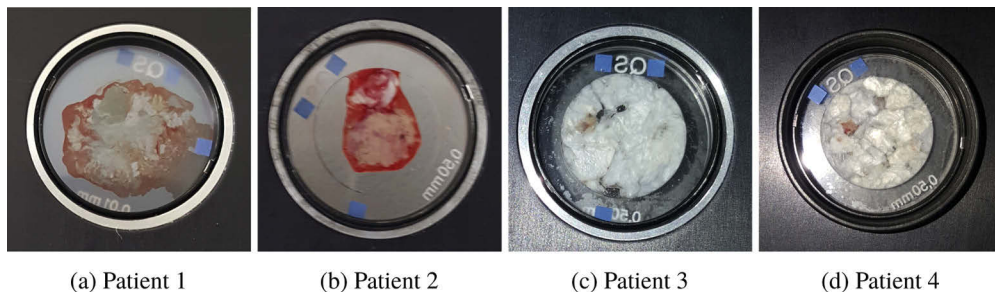
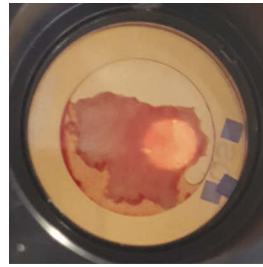


Fig. 2. This figure shows cholesteatoma samples of the four patients. The sample of (a) patient 1 and (b) patient 2 contain blood due to the extraction process, while the samples of (c) patient 3 and (d) patient 4 are nearly free of blood.



(a) Patient 1



(b) Patient 2

Fig. 3. Two analyzed bone chip samples of patient 1 and 2, respectively. The sample of patient 1 (a) contains a non-negligible amount of blood, while in the sample of patient 2 (b) nearly no blood is visible.

The measured diffuse reflectance R_d of several bone samples is shown in Fig. 4. The general trend of all measured reflectance curves is similar, regardless of whether the samples were bone fragments or bone chips. For all bone chip samples, the sample parameter were comparable with $r \approx 10$ mm and $d \approx 0.5$ mm. The higher reflectance intensity for the bone fragment curve in the visible spectrum resulted from the solid structure. The bone chip samples showed a lower reflection, as the granularity had a significant influence on the reflection: the lower the granularity

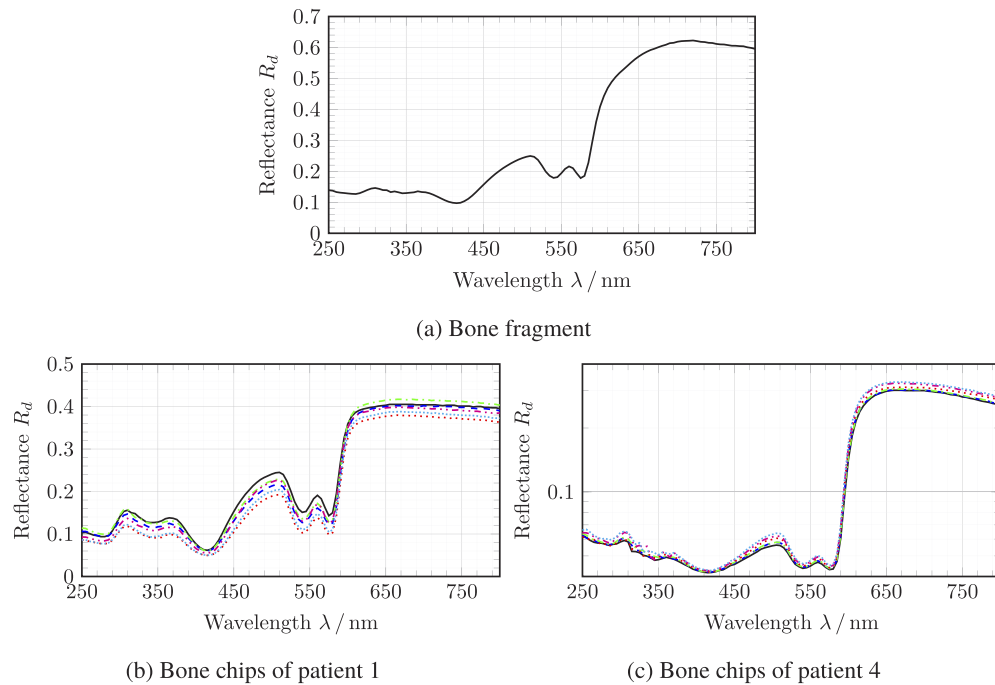


Fig. 4. These plots show the measured diffuse reflectance R_d of one bone fragment (a) and of twelve bone chip samples, six from patient 1 (b) and patient 4 (c), respectively. Each curve in the plots corresponds to one measured sample spectrum. The trend of all curves is similar, but the intensity of reflectance R_d differs. This is a result of the different sample quality, i.e. the bone fragment (a) as well as the bone chips (b) and (c) show different granularity, which effects the reflectance measurements.

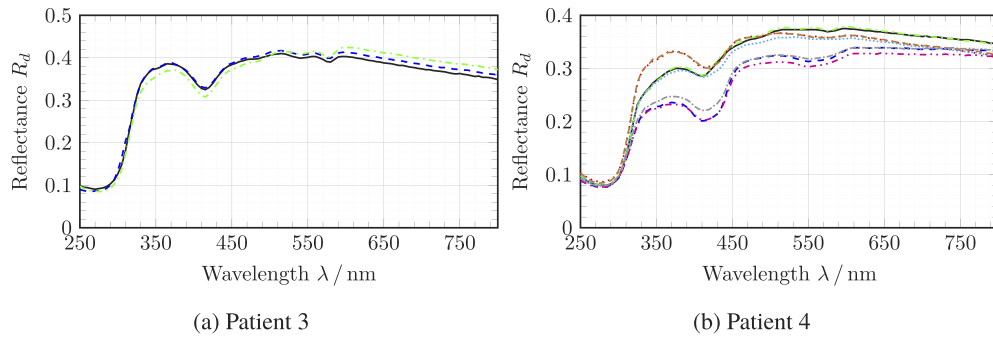


Fig. 5. These plots show measured reflectance R_d of cholesteatoma samples of two patients, P3 (a) and P4 (b). Each curve in the plots corresponds to one measured sample spectrum of the specific patient.

the higher the reflectance. Therefore, the reflectance is highest for the bone fragment and varies from patient to patient for the chip samples. Starting in the UV spectrum, the reflectance for bone is low and homogenous until about $\lambda \approx 590$ nm. For bone chips the curve progression is less homogenous in that spectral region, as the samples were contaminated with blood due to the extraction procedure, cf. Fig. 3(a).

The cholesteatoma samples had thicknesses of about $d \approx 0.5$ mm, while the size of the samples spread between $r = 5.3$ mm and $r = 15.0$ mm. Figure 5 shows exemplary the measured diffuse reflectance R_d of the cholesteatoma samples of patients 3 and 4. Both plots show the same reflectance behavior for cholesteatoma, where high homogenous reflectance over the entire analyzed spectrum from 280 nm to 800 nm is visible. In the range of 300 nm to 380 nm the reflectance intensity R_d is in the range of 0.23 to 0.34. Starting at ≈ 450 nm, R_d is about 0.30 to 0.45. These measured reflectance intensities correspond to measured epidermis reflectance with the difference that for the analyzed skin epidermis at approx. 550 nm an increase in reflectance of about 15% can be observed [28,29], while R_d of cholesteatoma shows a small depression in this area continuing homogeneously afterward, cf. Fig. 5.

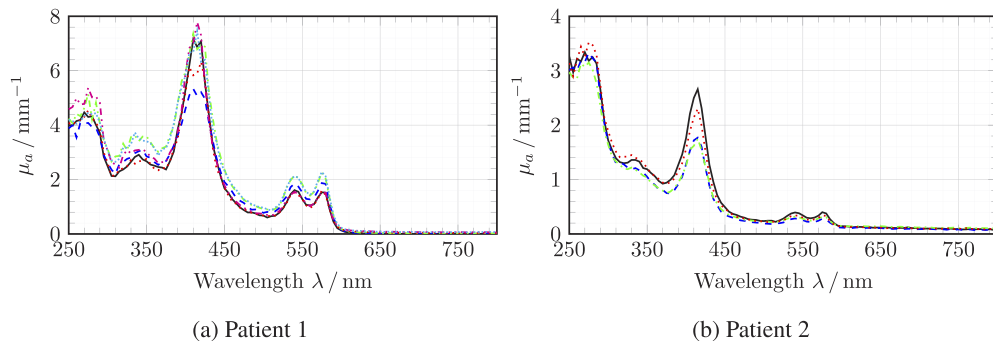


Fig. 6. These two plots exemplary show the results of the absorption coefficient μ_a of bone chips samples of patient 1 (a) and patient 2 (b). Each curve in the plots corresponds to one measured sample spectrum of the specific patient. As it can be seen at the peaks at 430 nm and around 550 nm, the influence of blood present in the sample plays a role for the results. In the sample of patient 1 (a) were more blood present as in the sample of patient 2 (b), cf. Fig. 3

3.2. Determination of the optical parameters

The simulated absorption coefficient μ_a of the bone chips (shown in Fig. 6) exhibit a clear peak at 430 nm and a double peak in the area of 550 nm. This behavior correlates to hemoglobin (Hb) and is resulting of the blood contamination of the bone chips samples with a stronger peak for patient 1 than for patient 2. As bone chips were analyzed, it could not be excluded that blood penetrates the sample during extraction. This blood affected the measurements and results. In the samples of patient 1 more blood was included than in the samples of patient 2, also shown in Fig. 3, which explains the different intensity of the Hb-peaks in the spectra. Besides the Hb-peaks, the spectra are comparable in trend and intensity of μ_a for all patients. A small peak exists between 330 nm and 340 nm and the plateau in the UV spectrum is at a similar range.

For the cholesteatoma samples, the absorption coefficient μ_a results are shown in Fig. 7. The samples of patient 1 and 2 show clear Hb-peaks at about 430 nm and 555 nm. This is again caused by the fact that these samples contained blood due to the extraction process, see Fig. 2. In the samples of patient 3 and 4 almost no blood was present, which results in a more uniform curve with high intensity of μ_a in the UV range, strong drop at about 300 nm and uniform decreasing of μ_a from 350 nm to 800 nm. This behavior corresponds with published epidermal tissue data [30].

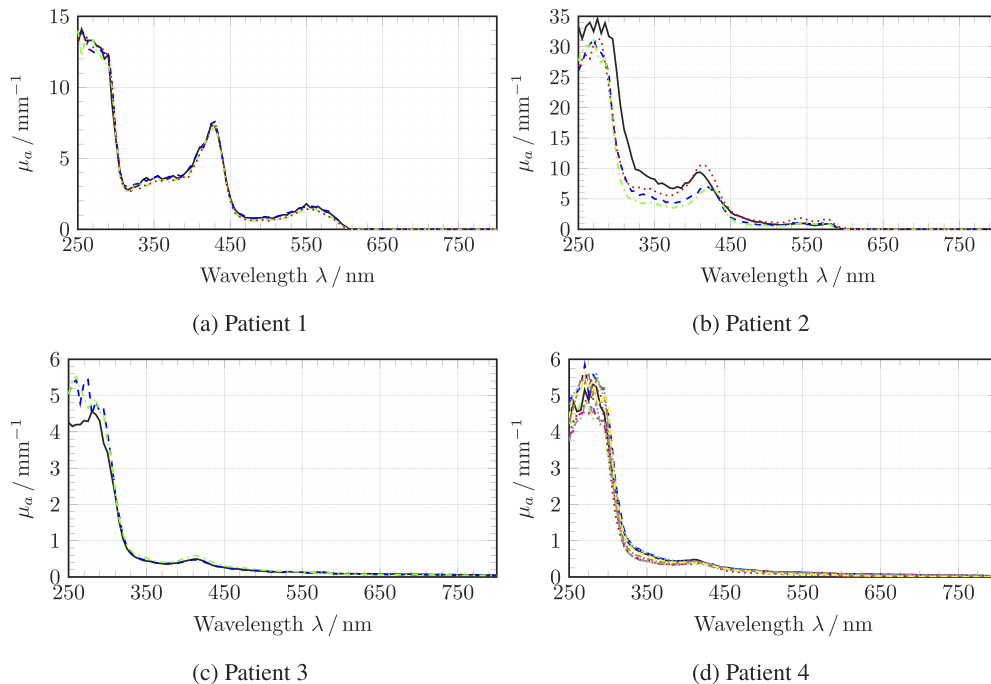


Fig. 7. All plots show the results of the absorption coefficient μ_a of cholesteatoma of the four analyzed patients in the measured range of 250 nm to 800 nm. Each curve in the plots corresponds to one measured sample spectrum of the specific patient. The samples of patient 1 (a) and patient 2 (b) contained blood, where the samples of patient 2 (b) contained much more blood. The samples of patient 3 (c) and patient 4 (d) were nearly freed of blood, cf. Fig. 2.

Further, the cholesteatoma and bone chips samples of patient 3 and 4 were not only analyzed directly after extraction but also after 20 h and 90 h, respectively. In contrast to the results presented in Wisotzky et al. [24] for soft tissue, no decreasing of μ_a over time could be observed for both analyzed tissue types. This effect had been expected, since this study, unlike the previous one, did not examine soft tissue but cholesteatoma and bone.

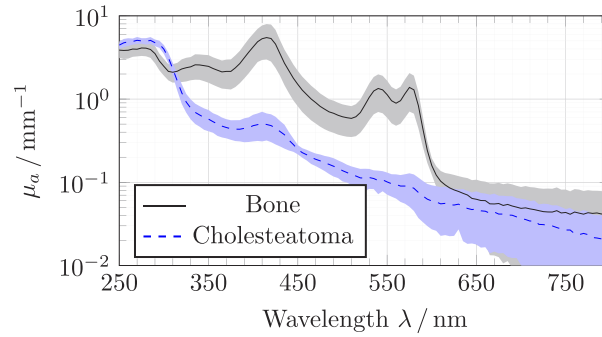


Fig. 8. The plot shows the results of the average absorption coefficient μ_a of cholesteatoma and bone in the measured range of 250 nm to 800 nm for comparison. The dark curve shows the average progression of all analyzed samples of each tissue type and the brighter trend characterizes the standard deviation of the simulated results.

Figure 8 plots the average optical absorption coefficient μ_a of the analyzed tissue types cholesteatoma ($n = 28$) and bone ($n = 16$). In the range starting at 310 nm up to 600 nm both tissue types show a distinct difference. The absorbency of cholesteatoma is about one order of magnitude lower than for bone chips. At 600 nm, μ_a of both tissue types are converging. The mean relative SDs for μ_a is 0.065 for the bone samples and 0.119 for the cholesteatoma samples.

The scattering was analyzed using the reduced scattering coefficient $\mu'_s = \mu_s(1 - g)$. The simulated scattering curves of the bone chips samples (see Fig. 9) show a continuously decrease of μ'_s over the complete spectrum. The magnitudes are the same over all patients, with approx. 10 mm^{-1} at 250 nm decreasing to approx. 5 mm^{-1} at 800 nm. Thus, the blood in the samples has a much smaller influence on the results of μ'_s than on the results of μ_a , cf. Fig. 6.

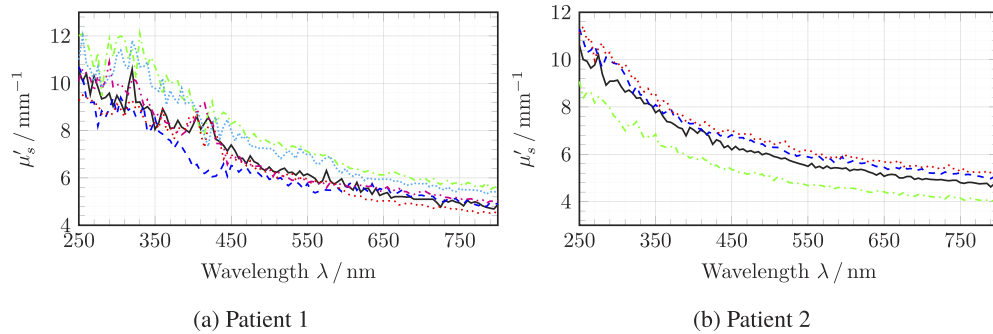


Fig. 9. In this plots the results of the scattering coefficient μ'_s of bone chips samples from patient 1 (a) and patient 2 (b) are shown. Each curve in the plots corresponds to one measured sample spectrum of the specific patient. In contrast to the results of μ_a , the effect of the blood in the samples is less strong and all spectra of both patients behave similar in shape and magnitude.

For the cholesteatoma samples, the scattering coefficient μ'_s form a plateau with an intensity of approx. 10 mm^{-1} in the analyzed UV range (250 nm to 300 nm), see Fig. 10. Then the curve rises steeply, up to 14.3 mm^{-1} at about $\lambda = 310 \text{ nm}$ to decrease then continuously like the bone chips samples. At 800 nm μ'_s is between 3 mm^{-1} and 4 mm^{-1} . In Fig. 10(b) four samples are plotted, analyzed at three different time points, directly after, 20 h and 90 h after extraction, respectively. It is visible, that the steep increase at about $\lambda = 310 \text{ nm}$ inverts its behavior to a steep decrease at about $\lambda = 310 \text{ nm}$, while the plateau in the UV range remains constant.

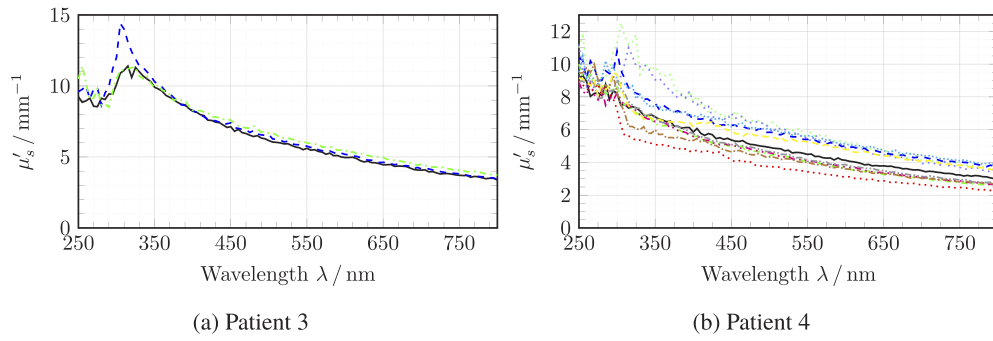


Fig. 10. All plots show the results of the scattering coefficient μ'_s of cholesteatoma of the analyzed blood-free samples in the measured range of 250 nm to 800 nm. Each curve in the plots corresponds to one measured sample spectrum of the specific patient. In plot (b) patient 4, the curves correspond to different measurement times after sample preparation ('—' directly after, '---' 20 h after and '...' 90 h after preparation, respectively).

Fig. 11 plots the average optical reduced scattering coefficient μ'_s of the analyzed tissue types cholesteatoma and bone. For both tissue types, μ'_s decreases continuously starting at 310 nm. The decreasing of μ'_s of cholesteatoma is higher than for bone chips. The scattering coefficient μ'_s of cholesteatoma shows at 310 nm a distinguish peak. The mean relative SDs for μ_a is 6.5% for the bone samples and 10.8% for the cholesteatoma samples.

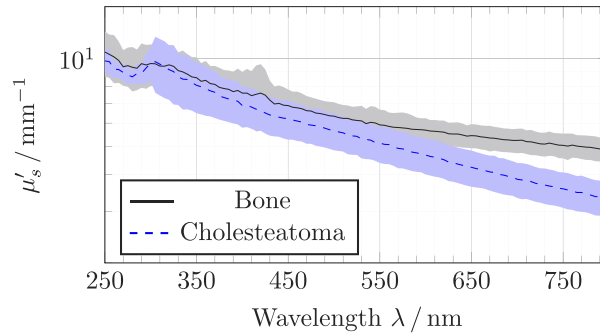


Fig. 11. The plot shows the results of the average reduced scattering coefficient μ'_s of cholesteatoma and bone in the measured range of 250 nm to 800 nm for comparison. The dark curve shows the average progression of all analyzed samples of each tissue type and the brighter trend characterizes the standard deviation of the simulated results.

As this is the first time that cholesteatoma was analyzed spectroscopically and cholesteatoma consists of keratinized stratified squamous epithelium like the epidermis, we compare our results to published epidermal μ_a and μ'_s in literature. As described above the principle reflectance behavior corresponds to epithelium. Additionally, the trend of the absorption coefficient μ_a as well as the reduced scattering coefficient μ'_s correspond to the literature, see Fig. 12.

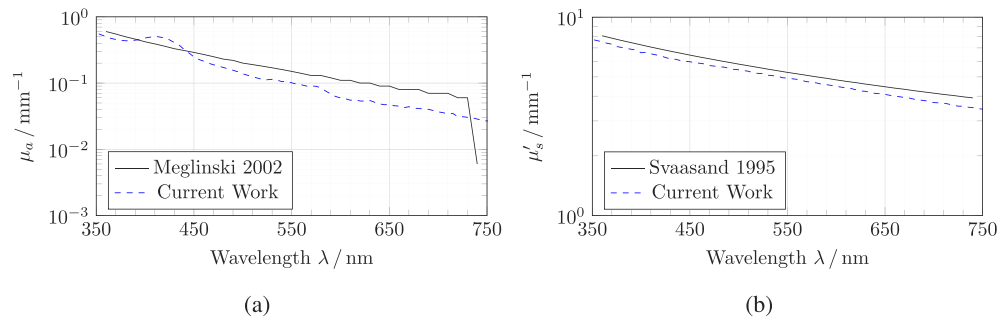


Fig. 12. The plots show the results of (a) the average absorption coefficient μ_a and (b) the average reduced scattering coefficient μ'_s of cholesteatoma compared to the results of epidermis presented by Meglinski & Matcher 2002 [31] for μ_a and Svaasand et al. 1995 [28] for μ'_s .

4. Discussion and conclusion

In this study, a high precision integrating sphere setup for measuring R_d and T_t in combination with a high resolving iMCS is used to determine the intrinsic optical parameters μ_a and μ'_s of human cholesteatoma and bone chips in the wavelength range 250 nm to 800 nm. This is in contrast to most of the data on tissue behavior presented in literature, which are mostly concerning the IR range. As the visible range is of high interest to the surgeon to carry out daily diagnostic and therapeutic interventions with or without microscopic and endoscopic support, this is the spectral range of interest in this study. Further, R_d has been measured of human bone fragments to distinguish differences in terms of reflection R_d between solid bone fragments and grind bone chips.

Although there are published results on fat, blood and skin, there is still insufficient data for various other tissue types that are important to clinicians and surgeons. This study aims at reducing this gap significantly, together with Wisotzky et al. [24]. The optical behavior of cholesteatoma in the visible range has not been described before. Due to the fact that the total removal of cholesteatoma with preservation and restoration of the ear function requires a high level of surgical expertise, there is a strong need for data on optical behavior. This study could help with the development of visual tools for better detection of cholesteatoma intraoperatively, which would result in better surgical outcomes and lower the number of revision surgeries. Nowadays, about one in five patients undergoes a revision surgery due to cholesteatoma [32,33].

Since no in-vivo measurements are possible due to the measurement setup, but in-vivo tissue properties however being of clinical interest, the samples are prepared and measured immediately after collection. In addition, it is shown that degradation of the tissue causes the reduced scattering coefficient μ'_s to drop in the near-UV and visible range starting at about $\lambda = 310$ nm. Thus, the principle in-vivo tissue properties can be deduced from the presented results, as the measurements are carried out next to the surgery site with minimal time delay [34].

We have shown that fundamental variances exist between human bone and cholesteatoma in the analyzed spectrum. Especially large differences in the specific tissue behavior (i.e. the measured reflectance values R_d as well as the determined optical parameters μ_a and μ'_s) in the range of 300 nm up to 600 nm have been detected. Additionally, differences between cholesteatoma and published epidermal data could be observed in terms of R_d , though both tissues consists of epithelium. These presented differences in the optical parameters substantiate the possibility to detect and identify, automatically or semi-automatically, tissue types for active treatment decisions during image-guided surgery [13,35,36]. Intraoperative tissue properties can be analyzed using multispectral imaging to point out tissue differences in the visualization process by using the

knowledge acquired in this study. Furthermore, it seems possible to use the presented results to train a classifier that makes tissue types more distinguishable intraoperatively. During training, the presence of blood in the situs has to be taken into account. This could be achieved by defining several possible tissue compositions including the relevant tissue types and using forward Monte Carlo simulation on the optical properties to simulate the diffuse reflectance as training data.

Funding

VW foundation (93927); Bundesministerium für Bildung und Forschung (16SV8061).

Acknowledgments

The authors wish to thank the Center of Experimental and Applied Cutaneous Physiology, Charité – Universitätsmedizin, Campus Mitte, Berlin, Germany as well as Prof. Dr. Meinke for providing the spectrometer and having such fruitful discussions.

Disclosures

The authors declare no conflicts of interest.

References

1. F. C. Uecker, *Hals-Nasen-Ohren-Heilkunde in Frage und Antwort: Fragen und Fallgeschichten zur Vorbereitung auf mündliche Prüfungen während des Semesters und Examen* (Elsevier, Urban & Fischer Verlag, 2006).
2. C. Dornelles, S. S. d. Costa, L. Meurer, and C. Schweiger, "Some considerations about acquired adult and pediatric cholesteatomas," *Rev. Bras. Otorrinolaringologia* **71**(4), 536–545 (2005).
3. D. R. Fassett, P. Kan, S. S. Chin, and W. T. Couldwell, "Cholesteatoma of the clivus," *Skull Base* **16**(1), 45–47 (2006).
4. H. Sudhoff and H. Hildmann, "Gegenwärtige theorien zur cholesteatomentstehung," *HNO* **51**(1), 71–83 (2003).
5. J. A. Smith and C. J. Danner, "Complications of chronic otitis media and cholesteatoma," *Otolaryngol. Clin. North Am.* **39**(6), 1237–1255 (2006).
6. P. Blanco, F. González, J. Holguín, and C. Guerra, "Surgical management of middle ear cholesteatoma and reconstruction at the same time," *Colomb. Med. (Cali)* **45**(3), 127–131 (2014).
7. E. Olszewska, M. Wagner, M. Bernal-Sprekelsen, J. Ebmeyer, S. Dazert, H. Hildmann, and H. Sudhoff, "Etiopathogenesis of cholesteatoma," *Eur. Arch. Oto-Rhino-Laryngology Head & Neck* **261**(1), 6–24 (2004).
8. T. Lister, P. A. Wright, and P. H. Chappell, "Optical properties of human skin," *J. Biomed. Opt.* **17**(9), 0909011 (2012).
9. S. L. Jacques, "Optical properties of biological tissues: a review," *Phys. Med. Biol.* **58**(11), R37–R61 (2013).
10. W.-F. Cheong, S. A. Prahl, and A. J. Welch, "A review of the optical properties of biological tissues," *IEEE J. Quantum Electron.* **26**(12), 2166–2185 (1990).
11. E. V. Salomatina, B. Jiang, J. Novak, and A. N. Yaroslavsky, "Optical properties of normal and cancerous human skin in the visible and near-infrared spectral range," *J. Biomed. Opt.* **11**(6), 064026 (2006).
12. G. Zonios and A. Dimou, "Light scattering spectroscopy of human skin in vivo," *Opt. Express* **17**(3), 1256–1267 (2009).
13. E. L. Wisotzky, F. C. Uecker, P. Arens, S. Dommerich, A. Hilsmann, and P. Eisert, "Intraoperative hyperspectral determination of human tissue properties," *J. Biomed. Opt.* **23**(9), 091409 (2018).
14. E. L. Wisotzky, B. Kossack, F. C. Uecker, P. Arens, S. Dommerich, A. Hilsmann, and P. Eisert, "Validation of two techniques for intraoperative hyperspectral human tissue determination," in *Proceedings of SPIE*, vol. 10951 (2019), p. 109511Z.
15. J. E. East, J. L. Vleugels, P. Roelandt, P. Bhandari, R. Bisschops, E. Dekker, C. Hassan, G. Horgan, R. Kiesslich, and G. Longcroft-Wheaton et al., "Advanced endoscopic imaging: European society of gastrointestinal endoscopy (esge) technology review," *Endoscopy* **48**(11), 1029–1045 (2016).
16. L. Svane-Knudsen, G. Halkier-Sørensen, P. Rasmussen, and V. D. Ottosen, "Cholesteatoma: a morphologic study of stratum corneum lipids," *Acta Oto-Laryngol.* **121**(5), 602–606 (2001).
17. B. M. Tissue, *Ultraviolet and Visible Absorption Spectroscopy* (American Cancer Society, 2012), pp. 1–13.
18. M. C. Meinke, G. J. Müller, J. Helfmann, and M. Friebe, "Optical properties of platelets and blood plasma and their influence on the optical behavior of whole blood in the visible to near infrared wavelength range," *J. Biomed. Opt.* **12**(1), 014024 (2007).
19. S. L. Jacques and B. W. Pogue, "Tutorial on diffuse light transport," *J. Biomed. Opt.* **13**(4), 041302 (2008).

20. M. Friebel, A. Roggan, G. J. Müller, and M. C. Meinke, "Determination of optical properties of human blood in the spectral range 250 to 1100 nm using monte carlo simulations with hematocrit-dependent effective scattering phase functions," *J. Biomed. Opt.* **11**(3), 034021 (2006).
21. A. Roggan, M. Friebel, K. Dörschel, A. Hahn, and G. J. Mueller, "Optical properties of circulating human blood in the wavelength range 400-2500 nm," *J. Biomed. Opt.* **4**(1), 36-47 (1999).
22. A. N. Yaroslavsky, I. V. Yaroslavsky, T. Goldbach, and H.-J. Schwarzmaier, "Optical properties of blood in the near-infrared spectral range," in *Optical Diagnostics of Living Cells and Biofluids*, vol. 2678 (International Society for Optics and Photonics, 1996), pp. 314-325.
23. L. L. Levy, N. Jiang, E. Smouha, R. Richards-Kortum, and A. G. Sikora, "Optical imaging with a high-resolution microendoscope to identify cholesteatoma of the middle ear," *The Laryngoscope* **123**(4), 1016-1020 (2013).
24. E. L. Wisotzky, F. C. Uecker, S. Dommerich, A. Hilsmann, P. Eisert, and P. Arens, "Determination of optical properties of human tissues obtained from parotidectomy in the spectral range of 250 to 800 nm," *J. Biomed. Opt.* **24**(12), 1-7 (2019).
25. M. Friebel, J. Helfmann, U. Netz, and M. C. Meinke, "Influence of oxygen saturation on the optical scattering properties of human red blood cells in the spectral range 250 to 2000 nm," *J. Biomed. Opt.* **14**(3), 034001 (2009).
26. A. Roggan, O. Minet, C. Schröder, and G. Müller, "Measurements of optical tissue properties using integrating sphere technique," in *Medical optical tomography: functional imaging and monitoring*, vol. 10311 (International Society for Optics and Photonics, 1993), p. 103110A.
27. W. H. Press, W. H. Press, B. P. Flannery, B. P. Flannery, S. A. Teukolsky, W. T. Vetterling, and W. T. Vetterling, *Numerical recipes in Pascal: the art of scientific computing*, vol. 1 (Cambridge University Press, 1989).
28. L. O. Svaasand, L. Norvang, E. Fiskerstrand, E. Stopps, M. Berns, and J. Nelson, "Tissue parameters determining the visual appearance of normal skin and port-wine stains," *Lasers Med. Sci.* **10**(1), 55-65 (1995).
29. R. Marchesini, C. Clemente, E. Pignoli, and M. Brambilla, "Optical properties of in vitro epidermis and their possible relationship with optical properties of in vivo skin," *J. Photochem. Photobiol., B* **16**(2), 127-140 (1992).
30. M. Van Gemert, S. L. Jacques, H. Sterenborg, and W. Star, "Skin optics," *IEEE Trans. Biomed. Eng.* **36**(12), 1146-1154 (1989).
31. I. V. Meglinski and S. J. Matcher, "Quantitative assessment of skin layers absorption and skin reflectance spectra simulation in the visible and near-infrared spectral regions," *Physiol. Meas.* **23**(4), 741-753 (2002).
32. R. Jackson, A. Addison, and P. Prinsley, "Cholesteatoma in children and adults: are there really any differences?" *J. Laryngol. Otol.* **132**(7), 575-578 (2018).
33. M. Stankovic, "Follow-up of cholesteatoma surgery: open versus closed tympanoplasty," *ORL* **69**(5), 299-305 (2007).
34. E. Salomatina and A. Yaroslavsky, "Evaluation of the in vivo and ex vivo optical properties in a mouse ear model," *Phys. Med. Biol.* **53**(11), 2797-2807 (2008).
35. E. Wisotzky, P. Arens, F. C. Uecker, A. Hilsmann, and P. Eisert, "A hyperspectral method to analyze optical tissue characteristics in vivo," *Int. J. Comput. Assist. Radiol. Surg.* **13**, S46-S47 (2018).
36. E. L. Wisotzky, J.-C. Rosenthal, F. Schmid, M. Bauer, P. Eisert, A. Hilsmann, A. Schneider, and F. C. Uecker, "Interactive and multimodal-based augmented reality for remote assistance using a digital surgical microscope," in *IEEE Conference on Virtual Reality and 3D User Interfaces (VR)*, vol. 26 (2019), pp. 1477-1484.